

Figure 4 Resistivity (ρ) of $\text{Na}_x\text{CoO}_2 \cdot y\text{H}_2\text{O}$ under zero magnetic field. The inset figure shows the resistivity measured under various magnetic fields. The electric resistivity was measured on a compressed powder sample by a standard four-probe method using a physical property measurement system (PP700C1, Quantum Design).

observed in the zero-field cooling process. We conclude that the present phase undergoes superconducting transition at about 5 K, because only superconductivity can account for such a large diamagnetism. With increasing H to 1 kOe, the onset temperature of superconductivity (onset T_c) did not change noticeably. With further increase of H up to 70 kOe, downturn of the susceptibility was still observed near 5 K, but the superconducting transition became quite broad and susceptibility was not negative even at 2 K. The M (magnetization)– H curve at 2 K, which is not shown here, indicated that the present material is a superconductor of the second kind with a lower critical field of around 100 Oe. The normal-state susceptibility depended on temperature, and decreased with increasing external magnetic field. $\text{Na}_{0.5}\text{CoO}_2$ shows Curie–Weiss-like magnetic behaviour rather than Pauli paramagnetic behaviour⁵. This suggests that the aforementioned normal-state magnetism reflects the intrinsic nature of the CoO_2 layer, although there is a possibility that the present sample contained a trace amount of magnetic impurity.

The electric resistivity (ρ) of $\text{Na}_x\text{CoO}_2 \cdot y\text{H}_2\text{O}$ is shown in Fig. 4. For the present system, it was impossible to prepare a tightly sintered ceramic specimen for the resistivity measurement. Instead, we measured a specimen obtained by room-temperature compression, and zero resistivity was not attained down to 2 K owing to this limitation. Nevertheless, a sharp decrease of resistivity was observed at around 4 K, supporting the superconducting transition. The onset temperature of 4 K is slightly lower than the value determined by the magnetic measurement, and this difference may be due to the variation of water content in the sample. The H_2O content was dependent on the humidity in the atmosphere, and superconductivity was greatly suppressed in a low H_2O -content sample. The superconducting transition became broad with an increasing magnetic field, as shown in Fig. 4, and no decline of resistivity was observed above 50 kOe. This presumably reflects the weak link nature of the specimen. It is, however, worth noting that the onset T_c does not appear to depend significantly on the magnetic field. For instance, onset T_c at 10 kOe was very close to that under zero field.

There is a marked resemblance between the present cobalt oxide and high- T_c copper oxides. In the high- T_c copper oxides, superconductivity occurs in the CuO_2 square lattice. The Cu^{2+} ($S = 1/2$) moments are antiferromagnetically ordered in the CuO_2 plane. With a low level of carrier (hole or electron) doping, the antiferro-

magnetism is suppressed drastically, and the system becomes metallic, followed by the appearance of superconductivity. By analogy, the present material may be understood to be an electron-doped system for a low-spin Co^{4+} ($S = 1/2$) lattice with an electron density (x in $\text{Na}_x\text{CoO}_2 \cdot y\text{H}_2\text{O}$) of around 0.35 per Co atom. As shown in Figs 3 and 4, the increasing external magnetic field broadened the superconducting transition but did not markedly lower the onset T_c . Similar behaviour is always observed in high- T_c copper oxides.

The strong 2D character of the layered copper oxides is believed to be important in superconductivity. In the same way, the large separation of the CoO_2 layers by the introduction of H_2O molecules seems to be essential for inducing superconductivity in the present material (superconductivity is greatly suppressed by the removal of water, accompanied by a shrinkage of the c axis). The main difference between the two systems is that Co ions form a triangular lattice with magnetically frustrated geometry in contrast to the square lattice of the CuO_2 plane. Further studies are needed to elucidate the mechanism of superconductivity. □

Received 18 October 2002; accepted 28 January 2003; doi:10.1038/nature01450.

1. Bednorz, J. G. & Müller, K. A. Possible high T_c superconductivity in the Ba-La-Cu-O system. *Z. Phys. B* **64**, 189–193 (1986).
2. Fouassier, C., Matejka, G., Reau, J.-M & Hagenmüller, P. Sur de nouveaux bronzes oxygènes de formule Na_xCoO_2 ($x \leq 1$). Le système cobalt-oxygène-sodium. *J. Solid State Chem.* **6**, 532–537 (1973).
3. Balsys, R. J. & Davis, R. L. Refinement of the structure of $\text{Na}_{0.74}\text{CoO}_2$ using neutron powder diffraction. *Solid State Ionics* **93**, 279–282 (1996).
4. Izumi, F. & Ikeda, T. A Rietveld-analysis program RIETAN-98 and its applications to zeolites. *Mater. Sci. Forum* **321–324**, 198–203 (2000).
5. Tanaka, T., Nakamura, S. & Iida, S. Observation of distinct metallic conductivity in NaCo_2O_4 . *Jpn J. Appl. Phys.* **33**, L581–L582 (1994).

Acknowledgements We thank Y. Yajima, S. Takenouchi and H. Komori of our institute for IR, ICP-AES and EDX analysis.

Competing interests statement The authors declare that they have no competing financial interests.

Correspondence and requests for materials should be addressed to K.T. (e-mail: takada.kazunori@nims.go.jp).

..... Dynamical coupling of wind and ocean waves through wave-induced air flow

T. S. Hristov*, S. D. Miller† & C. A. Friehe†‡

* Department of Earth and Planetary Sciences, Johns Hopkins University, Baltimore, Maryland 21218, USA

† Department of Earth System Science, ‡ Department of Mechanical and Aerospace Engineering, University of California, Irvine, California 92697, USA

Understanding the physical mechanisms behind the generation of ocean waves by wind has been a longstanding challenge^{1,2}. Previous studies^{3–6} have assumed that ocean waves induce fluctuations in velocity and pressure of the overlying air that are synchronized with the waves, and numerical models have supported this assumption⁷. In a complex feedback, these fluctuations provide the energy for wave generation. The spatial and temporal structure of the wave-induced airflow therefore holds the key to the physics of wind–wave coupling, but detailed observations have proved difficult. Here we present an analysis of wind velocities and ocean surface elevations observed over the open ocean. We use a linear filter⁸ to identify the wave-induced

air flow from the measurements and find that its structure is in agreement with ‘critical-layer’ theory³. Considering that the wave-induced momentum flux is then controlled by the wave spectrum and that it varies considerably in vertical direction, a simple parametrization of the total air–sea momentum flux is unlikely to exist.

Over the ocean, turbulent pressure fluctuations in the air initiate small ripples on the water surface⁹ that further grow and develop into wind-driven waves through a poorly understood mechanism. Once present, the surface waves profoundly affect the exchange of momentum and kinetic energy at the air–sea interface. Although experiments have detected strong variability of the interfacial fluxes with sea state, both a clear phenomenological description of the fluxes and insight into the mechanism of exchange have remained elusive^{10–12}. Incomplete understanding of the air–sea interaction reduces the predictive power of climate models as well as of weather and wave forecasts.

The concept of resonant wind–wave interaction assumes that the waves induce velocity $\tilde{\mathbf{v}}$ and pressure \tilde{p} fluctuations in the wind, that in a broad sense are synchronized with the waves. Considering collinear wind and waves, the wind velocity \mathbf{v} is a sum of turbulent fluctuations $\mathbf{v}' \equiv (u', v', w')$ and wave effects $\tilde{\mathbf{v}} \equiv (\tilde{u}, 0, \tilde{w})$, both superimposed on a long-term mean horizontal velocity $\mathbf{U} = (U, 0, 0)$ so that $\mathbf{v} = \mathbf{U} + \mathbf{v}' + \tilde{\mathbf{v}}$. The same decomposition applies to the pressure: $p = P + p' + \tilde{p}$. When the perturbed pressure \tilde{p} is lower on the lee side and higher on the windward side of the wave, the perturbation delivers energy from the air flow to the waves at a

rate $\tilde{E} = \langle \tilde{p}_0 \tilde{\eta} \rangle$ (\tilde{p}_0 is the pressure and $\tilde{\eta}$ is the velocity at the interface). The spatio-temporal structure of the wave-induced flow uniquely describes the mechanism of coupling, determines the air pressure distribution on the interface¹³, and therefore the wave growth rate. Agreement between theoretically derived and experimentally observed flow structures would present a conclusive validation for the theory predicting the flow structure. In contrast, because the interfacial pressure distribution does not uniquely determine the overlying flow structure, agreement between measured and predicted wave growth rates only is insufficient to confirm experimentally a wind–wave interaction model¹⁴.

The critical-layer theory³ builds on the concept of resonant wind–wave interaction. There, the turbulent atmospheric flow is considered to be of constant stress $\tau(z) \equiv -\rho \langle u' w' \rangle = \rho u_*^2 = \text{Const.}$, so the mean-wind vertical profile is logarithmic¹⁵ $U(z) = (u_* / \kappa) \log(z/z_0)$. (Here, ρ is the air density, u_* is the friction velocity, z_0 is the ocean surface roughness scale, κ is the von Karman constant, and z is the distance from the unperturbed air–water interface.) The surface waves are generated as growing perturbations of the mean flow $U(z)$, while no wave–turbulence interaction is assumed to occur (quasi-laminar approximation). Because of the large Reynolds number of the wind over the ocean, viscosity is neglected. Within these assumptions the perturbation stream function $\psi(z)$ satisfies the Rayleigh equation^{3,16}:

$$\psi'' - k^2 \psi - U''(U - c)^{-1} \psi = 0 \quad (1)$$

Here $c = (g/k)^{1/2}$ is the phase speed of the wave mode $\eta = A e^{ik(x-ct)}$, k is its wavenumber and g is the acceleration of gravity. The parameter controlling the solution of equation (1), and therefore the wind–wave interaction, is the ratio c/u_* . For equation (1) the height z_c , where $U(z_c) = c$, known as the critical height, is a point of regular singularity. Velocity and pressure fields, obtained from solving equation (1), result in these wind-to-wave fluxes of energy

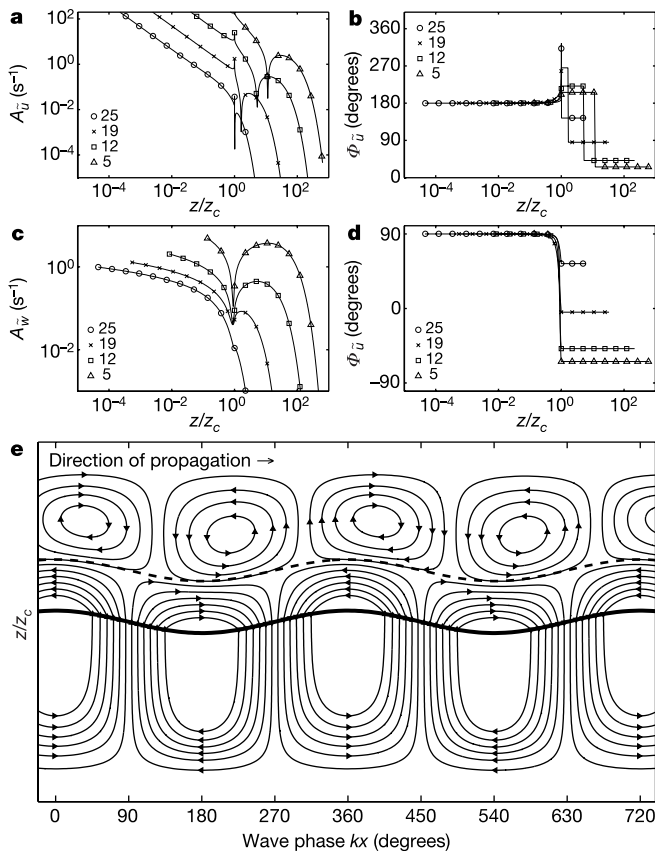


Figure 1 Numerical solutions for the Rayleigh equation (1). **a, b**, Amplitude $A_{\tilde{u}}$ (**a**) and phase $\Phi_{\tilde{u}}$ (**b**) of the horizontal wave-induced velocity fluctuations $\tilde{u}(z/z_c)$. **c, d**, Amplitude $A_{\tilde{w}}$ (**c**) and phase $\Phi_{\tilde{w}}$ (**d**) of the vertical wave-induced velocity fluctuations $\tilde{w}(z/z_c)$. Each curve corresponds to a value of the parameter c/u_* , as indicated in the symbol key. The flow streamlines (**e**) have been reconstructed from the solution ψ for $c/u_* = 5.75$. The solid line represents the air–water interface and the dashed line is the critical height. The whole eddy structure is propagating to the right following the wave. k is wavenumber.

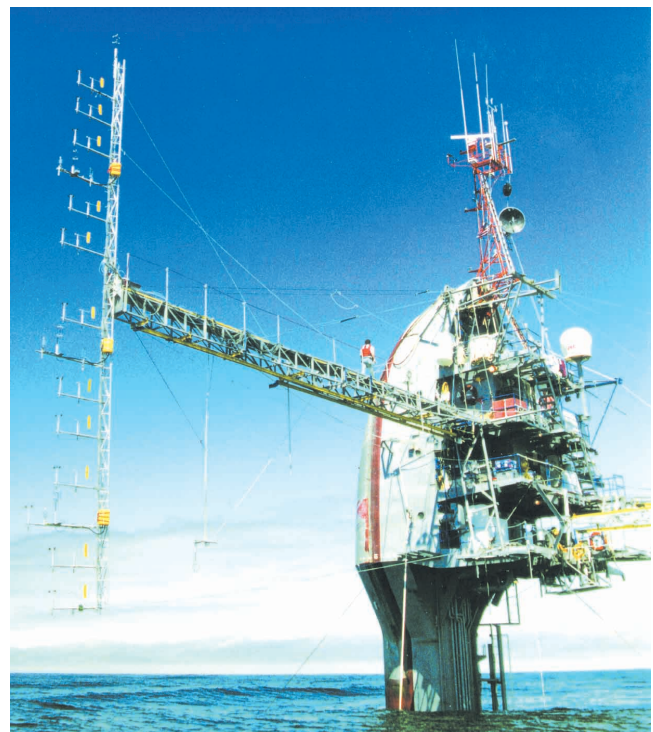


Figure 2 Floating Instrument Platform *FLIP* moored during the experiment. Four ultrasonic anemometers measured the wind velocity at different heights above the ocean surface and 12 cup anemometers and vanes registered the horizontal wind speed and direction. The sea surface elevation was measured beneath the mast.

$\tilde{E} = -(\pi/2)(u_*/k)^2 \rho k c |\eta|^2 |\psi(z_c)|^2 U''(z_c)/U'(z_c)$, and momentum $\tilde{\tau} \equiv -\rho(\tilde{u}\tilde{w}) = \tilde{E}/c$. The dependence of \tilde{E} and $\tilde{\tau}$ on quantities at the critical height z_c indicates that wind-wave energy and momentum exchanges are formally occurring in a thin layer about z_c , known as the critical layer^{3,16}. Away from the critical height the singular term $U''\psi/(U-c)$ vanishes and the solutions are decaying exponents scaled by the wavelength $\psi \propto e^{-kz}$. Thus short (slow) wave signatures in the wind will be significant only close to the surface, while only fluctuations induced by the long (fast) waves will propagate further up.

The complex-valued solution $\psi(z, c/u_*)$ of equation (1) carries information about the wave-induced along-wind $\tilde{u} = -(u_*/k) \times (d\psi/dz)\eta$ and vertical $\tilde{w} = ik(u_*/k)\psi\eta$ velocity. Their normalized amplitudes $A_{\tilde{u}} = |\tilde{u}/\eta|$, $A_{\tilde{w}} = |\tilde{w}/\eta|$ and phases $\Phi_{\tilde{u}} = \arg(\tilde{u}/\eta)$, $\Phi_{\tilde{w}} = \arg(\tilde{w}/\eta)$ appear in Fig. 1. The solution predicts distinct features for the wave-induced flow at z_c : the phase $\Phi_{\tilde{w}}(z)$ is constant on both sides of z_c and discontinuous at z_c (Fig. 1d) and the amplitude $A_{\tilde{w}}(z)$ has a minimum near that point (Fig. 1c). The behaviour of \tilde{u} includes a pair of abrupt changes in amplitude (Fig. 1a) and phase (Fig. 1b) at and above z_c . We will seek to recognize these distinct

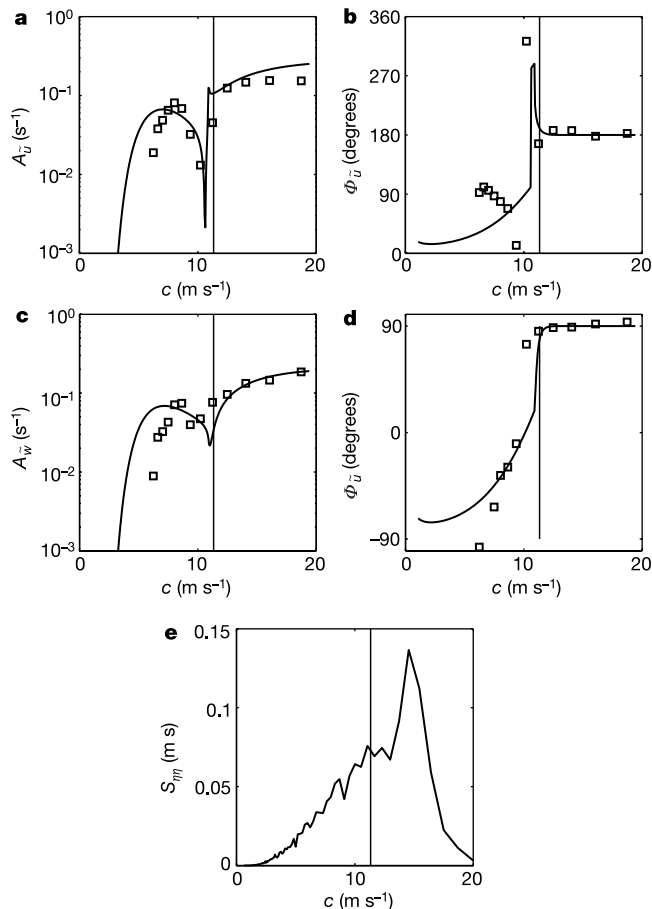


Figure 3 Theoretical and experimental transfer functions for the wave-coherent velocities $T_{\tilde{u}}(c) = A_{\tilde{u}}e^{i\Phi_{\tilde{u}}}$ and $T_{\tilde{w}}(c) = A_{\tilde{w}}e^{i\Phi_{\tilde{w}}}$ and a surface elevation power spectrum.

a, b, Amplitude $A_{\tilde{u}}$ (**a**) and phase shift $\Phi_{\tilde{u}}$ (**b**) for the along-wind wave-induced velocity fluctuations \tilde{u} . **c, d**, Amplitude $A_{\tilde{w}}$ (**c**) and phase shift $\Phi_{\tilde{w}}$ (**d**) for the vertical wave-induced velocity fluctuations \tilde{w} ; **(e)**, Surface wave power spectrum $S_{\eta\eta}$ versus the wave phase speed c . The amplitudes in **a** and **c** are normalized by the surface wave amplitude at that phase speed; the phases in **b** and **d** are referenced to the phase of the waves. The solid lines are numerical results from equation (1); the squares are experimental estimates from time series of wind velocity ($z_f = 8.7$ m) and wave elevation collected over 90 minutes. The vertical line marks the mean wind speed measured over the same time period, that is, it shows the wave mode for which the instrument is at the mode's critical height.

features of the wave-induced flow in our field experiment data. The spatial configuration of the wave-induced flow (Fig. 1e), reconstructed from the solutions of equation (1) (Fig. 1a–d), shows two eddy structures brought into contact at the critical height and the streamlines continuous through the air–water interface. A Fourier superposition of flows like the one in Fig. 1e forms the actual wave-induced flow over the sea.

Here we analyse data collected continuously over five days in May 1995 over the open ocean 50 km off Monterey, California, at water depth of 1,500 m from the stable research platform *FLIP* (Fig. 2). From a mast we measured the turbulent wind velocity with four ultrasonic anemometers (accuracy 3% of the instantaneous velocity) at fixed heights of 3.5, 8.7, 13.8 and 18.1 m above the mean ocean level, as well as the surface elevation η (accuracy, 1 cm) directly beneath the mast. The signals were sampled at 50 Hz. The slight motion of the platform was recorded and later removed from the measured wind velocities. During the experiment the conditions ranged from calm, with wind velocity at 10 m height $U_{10} = 2 \text{ m s}^{-1}$, to stormy, with $U_{10} = 14 \text{ m s}^{-1}$. Waves aligned with the wind developed in response to the increasing wind speed and maximum wave height reached 3 m. During the experiment, both u_* and the wave spectrum varied, providing a range of the controlling parameter c/u_* .

The wave-induced flow $\tilde{\mathbf{v}}$ in the wind has long been difficult to detect because turbulence \mathbf{v}' dominates and blurs any wave signature there^{17,18}. A robust and optimal method to separate \mathbf{v}' and $\tilde{\mathbf{v}}$ has been proposed⁸. The linearity of the Rayleigh equation (1) leads to the wave-induced velocity $\tilde{\mathbf{v}}$ being related to the wave elevation η by a linear transform, that is, $\tilde{\mathbf{v}}$ is coherent with η . Therefore, a filter separating $\tilde{\mathbf{v}}$ from \mathbf{v}' must also ensure that property of $\tilde{\mathbf{v}}$. As an estimate for $\tilde{\mathbf{v}}$, we choose the orthogonal projection of the wind signal \mathbf{v} onto the Hilbert space of all the wave-coherent signals. Such an estimate is optimal in the least-squares sense⁸.

Measurements of wind velocity were conducted at fixed heights and over a time period (90 minutes, in this case), they produce a single value of u_* , while the spectrum of waves provides a range of values for c . Therefore, comparison with our experiment requires consideration of the behaviour of $\tilde{u}(z, c/u_*)$ and $\tilde{w}(z, c/u_*)$ at fixed z and u_* and variable c . Introducing $S_{\alpha\beta}$ as the cross-spectral density of the time-series $\alpha(t)$ and $\beta(t)$ and the transfer functions $T_{\tilde{u}}(c) = S_{\eta\tilde{u}}/S_{\eta\eta}$ and $T_{\tilde{w}}(c) = S_{\eta\tilde{w}}/S_{\eta\eta}$, we estimate the normalized amplitudes ($A_{\tilde{u}} = |T_{\tilde{u}}|$ and $A_{\tilde{w}} = |T_{\tilde{w}}|$) and phases ($\Phi_{\tilde{u}} = \arg T_{\tilde{u}}$ and $\Phi_{\tilde{w}} = \arg T_{\tilde{w}}$) of the measured \tilde{u} and \tilde{w} .

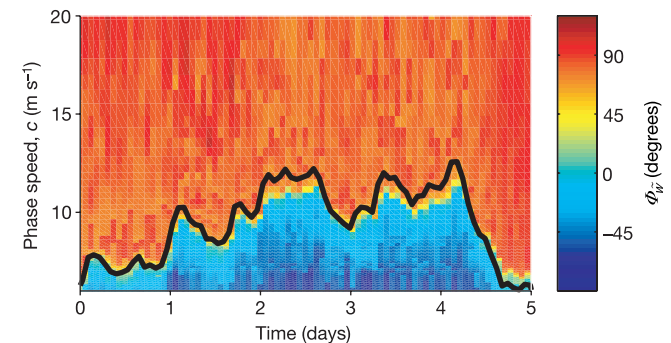


Figure 4 The measured phase of the vertical wave-induced velocity fluctuations $\Phi_{\tilde{w}}$ in degrees throughout a five-day period. The phase is referenced to the phase of the waves. The solid black line shows the mean wind speed $U(z)$ versus time, and also marks the wave mode $c = U(z)$, for which the instrument is at the mode's critical height. For modes faster than the mean wind the instrument is below their critical heights and for modes slower than the wind the instrument is above their critical heights. The line of the mean wind speed marks the persistent abrupt change in phase, as predicted by the solutions of the Rayleigh equation (1), and in agreement with Figs 1d and 3d. Data are from the anemometer at $z_f = 3.5$ m.

Figure 3 shows numerical results and the experimental estimates for the amplitude and phase of the horizontal and vertical wave-coherent wind velocities versus c at fixed z and u_* . For the numerical $\tilde{w}(z, c|u_*)$ at constant z and u_* the abrupt change of its phase is clearly recognizable (Fig. 3d), occurring at $c = U(z_i)$, z_i being the vertical position of the instrument. Indeed, for the wave mode $c = U(z_i)$ the instrument is at the mode's critical height; for all the slower modes $c < U(z_i)$ the instrument is above their critical heights ($z_i > z_c$), and for all faster modes $c > U(z_i)$ the instrument is below their critical heights ($z_i < z_c$). The numerical and the experimental results seem to agree closely and the distinct wave-induced flow features, such as the abrupt change of the phase and the minimum of the amplitude about $c = U(z_i)$, are clearly captured by the experimental data. Nonlinear interaction between wave modes transfers most of the wave energy to the long (fast) waves and leaves little energy in the short (slow) modes, as illustrated by the wave spectrum $S_{\eta\eta}(c)$ in Fig. 3e. Also, as the wave-induced field's vertical decay is scaled by the wavelength, at a given height z_i the shorter the wave the stronger the attenuation of the velocity induced by the wave. In combination, these two circumstances result in a low signal-to-noise ratio for the short-wave signature in the wind and greater uncertainty for the estimated amplitude and phase of the velocity induced by these short (slow) waves. Therefore, numerics and experiment show closer agreement for long (fast) waves and greater divergence for short (slow) waves (Fig. 3a–d).

Throughout the experiment the wave-induced flow maintains the critical layer pattern. That pattern is clearly observed in the phase of the vertical wave-induced velocity fluctuations (Fig. 4), which exhibits a distinct and persistent change along the mean wind line $c = U(z_i)$. For fast ($c > U(z_i)$) waves the phase remains close to 90° , while for waves slower than the mean wind ($c < U(z_i)$) it rapidly decreases, as predicted by the numerical results in Figs 1d and 3d.

Thus we identified the wave-induced flow from field measurements and showed that its configuration is closely consistent with the predictions of the critical-layer theory³ for the range $16 < c/u_* < 40$. Such a result confirms that for the resolved wave scales the critical-layer mechanism of wind–wave coupling is clearly active over the open ocean. Models of climate as well as weather and wave forecasting¹⁹ rely on current knowledge about air–sea fluxes as boundary conditions on the ocean–atmosphere interface. Data from measurements have been used in extensive efforts to parameterize the air–sea momentum flux by expressing the ocean surface drag coefficient $C_D = u_*^2/U^2$ through a single variable. There, the experimental points have systematically failed to collapse onto a particular curve^{10–12} and the observed scatter has not been reduced by accumulating more statistics and by improving the quality of measurements. The evidence presented here in support of the critical layer mechanism³ indicates (i) that the total wave-induced momentum flux $\tilde{\tau} \equiv -\rho\langle\tilde{u}\tilde{w}\rangle = \tilde{E}/c$ is controlled by the wave spectrum and not by a single representative parameter and (ii) that $\tilde{\tau}$ has a considerable vertical variability. These two circumstances are probably major contributors to the observed scatter of drag coefficient estimates. □

Received 24 May; accepted 17 December 2002; doi:10.1038/nature01382.

1. Thomson, W. (Lord Kelvin) Hydrokinetic solutions and observations. *Phil. Mag.* **42**(4), 362–377 (1871); *Math Phys. Pap.* **4**, 80.
2. Jeffreys, H. On formation of waves by wind. *Proc. R. Soc. Lond. A* **107**, 189–206 (1924).
3. Miles, J. W. On the generation of surface waves by shear flows. *J. Fluid Mech.* **3**, 185–204 (1957).
4. Belcher, S. & Hunt, J. C. R. Turbulent shear flow over slowly moving waves. *J. Fluid Mech.* **251**, 109–148 (1993).
5. Meirink, J. F. & Makin, V. Modelling low-Reynolds-number effects in the turbulent air flow over water waves. *J. Fluid Mech.* **415**, 155–174 (2000).
6. Li, P. Y., Xu, D. & Taylor, P. A. Second order turbulence closure modeling for air flow over water waves. *Boundary-Layer Meteorol.* **95**, 397–425 (2000).
7. Sullivan, P., McWilliams, J. & Moeng, C.-H. Simulation of turbulent flow over idealized water waves. *J. Fluid Mech.* **404**, 47–85 (2000).
8. Hristov, T., Friehe, C. & Miller, S. Wave-coherent fields in air flow over ocean waves: Identification of cooperative behavior buried in turbulence. *Phys. Rev. Lett.* **81**, 5245–5248 (1998).

9. Phillips, O. M. On the generation of waves by turbulent wind. *J. Fluid Mech.* **2**, 417–445 (1957).
10. Donelan, M. *Air–Sea Interaction* Vol. 9 (eds LeMehaute, B. & Hanes, D. M.), 239–292 (John Wiley & Sons, New York, 1990).
11. Komen, G., Cavaleri, L., Donelan, M., Hasselmann, K., Hasselmann, S. & Janssen, P. *Dynamics and Modelling of Ocean Waves* (Cambridge Univ. Press, Cambridge, UK, 1994).
12. Csanady, G. T. *Air–Sea Interaction: Laws and Mechanisms* (Cambridge Univ. Press, Cambridge, UK, 2001).
13. Longuet-Higgins, M. S. Action of variable stress at the surface of water waves. *Phys. Fluids* **12**, 737–740 (1969).
14. Davis, R. E. On the turbulent flow over a wavy boundary. *J. Fluid Mech.* **42**, 721–731 (1970).
15. Landau, L. D. & Lifshitz, E. M. *Fluid Mechanics* 172–176 (Pergamon, Oxford, 1986).
16. Lin, C. *The Theory of Hydrodynamic Stability* (Cambridge Univ. Press, Cambridge, 1955).
17. Phillips, O. M. *The Dynamics of the Upper Ocean* 108 (Cambridge Univ. Press, Cambridge, UK, 1977).
18. Hasse, L. & Dobson, F. *Introductory Physics of the Atmosphere and Ocean* 101 (D. Reidel Publ., Boston, 1986).
19. Janssen, P. et al. *Impact and Feedback of Ocean Waves on the Atmosphere* Vol. 1 of *Advances in Fluid Mechanics* Ch. 5 155–198 (WIT Press, Ashurst, 2002).

Acknowledgements J. Edson's help and the expert assistance of FLIP's captain Tom Golfinos and crew made it possible to carry out the experiment. In discussions, comments or criticisms came from O. Phillips, M. Donelan, J. McWilliams, P. Sullivan, J.C.R. Hunt, P. Taylor, M. McIntyre, S. Belcher, V. Makin and V. Kudryavtsev. ONR (Marine Meteorology) has provided the funding for this work.

Competing interests statement The authors declare that they have no competing financial interests.

Correspondence and requests for materials should be addressed to T. H. (e-mail: Tihomir.Hristov@jhu.edu).

Iron–silica interaction at extreme conditions and the electrically conducting layer at the base of Earth's mantle

L. Dubrovinsky*, N. Dubrovinskaia*, F. Langenhorst*, D. Dobson*, D. Rubie†, C. Gebmann†, I. A. Abrikosov‡, B. Johansson‡§, V. I. Baykov§, L. Vitos☆, T. Le Bihan¶, W. A. Crichton¶, V. Dmitriev# & H.-P. Weber#

* Bayerisches Geoinstitut, Universität Bayreuth, D-95440 Bayreuth, Germany

† Max-Planck-Institut für Chemie, Joh.-Joachim-Becher-Weg 27, 0-55128 Mainz, Germany

‡ Condensed Matter Theory Group, Department of Physics, Uppsala University, S-751 21 Uppsala, Sweden

§ Applied Materials Physics, Department of Materials Science and Engineering, Royal Institute of Technology, Brinellvägen 23, SE-100 44, Stockholm, Sweden

¶ Theoretical Physics Department, Moscow State Institute of Steel and Alloys, Leninskii pr., 4, 117936 Moscow, Russia

¶ European Synchrotron Radiation Facility,

Swiss-Norwegian Beam Lines at ESRF, F-38043 Grenoble, France

☆ Research Institute for Solid State Physics and Optics, H-1525 Budapest, P.O. Box 49, Hungary

The boundary between the Earth's metallic core and its silicate mantle is characterized by strong lateral heterogeneity and sharp changes in density, seismic wave velocities, electrical conductivity and chemical composition^{1–7}. To investigate the composition and properties of the lowermost mantle, an understanding of the chemical reactions that take place between liquid iron and the complex Mg-Fe-Si-Al-oxides of the Earth's lower mantle is first required^{8–15}. Here we present a study of the interaction between iron and silica (SiO₂) in electrically and laser-heated diamond anvil cells. In a multianvil apparatus at pressures up to 140 GPa and temperatures over 3,800 K we simulate conditions down to the core–mantle boundary. At high temperature and pressures below 40 GPa, iron and silica react to form iron oxide and an iron–silicon alloy, with up to 5 wt% silicon. At pressures